14 Phase Transitions, Materials and Applications

F. von Rohr, H. Grundmann, O. Bossen, K. Inderbitzin, S. Siegrist, A. Engel, and A. Schilling

in collaboration with Tohoku University (N. Toyota), Karlsruhe Institut für Technologie (K. Il'in), Deutsches Zentrum für Luft- und Raumfahrt (H.-W. Hübers, A. Semenov), FIRST Lab ETH Zürich, PSI Villigen (M. Medarde, K. Conder), McMaster University (H. Dabkowska), IFW Dresden (V. Kataev, A. Alfonsov), University of São Paulo (A. Paduan-Filho), Institute of Nuclear Physics, Tashkent (A. Rakhimov), ETH Zürich (R. Nesper), and Princeton University (R. J. Cava)

(PTMA)

14.1 Superconducting nanowire single-photon detectors for optical and X-ray photons

In the previous annual report we described the successful development and testing of an X-ray superconducting nanowire single-photon detector (X-SNSPD) from a 100 nm thick Nb film [1]. We observed ultrafast, dark count-free keV-photon detection and a significant dependence of the pulse amplitude distribution on the photon energy. However, this Nb X-SNSPD latched (i.e. was not operational) for bias currents larger than 5.5% of the critical current I_c, due to the low resistance of the normal domains forming in a Nb nanowire at photon detection.

In order to reduce this susceptibility to latching, TaN was used as a detector material, as it has an about two orders of magnitude larger resistivity and a larger keV X-ray absorptance and magnetic penetration depth (and thus leads to a larger detector kinetic inductance) than Nb. Two X-SNSPDs from a 100 nm thick TaN film were fabricated with different nanowire widths w (Fig. 14.1), TaN-A with $w \simeq 310$ nm and TaN-B with $w \simeq 1.85$ μm, and their properties were compared with those of the Nb X-SNSPD [2]. The TaN detectors indeed latch for significantly higher bias currents, at 52% I_c (TaN-A) and 32% I_c (TaN-B).

The increased resistivity of TaN also reduces the problem of differentiating small-amplitude photon detection pulses from electronic noise, and a device detection efficiency (DDE) of 1.4% for 5.9 keV photons was determined for TaN-A, which is significantly larger than the lower limit of 0.03% found for the Nb X-SNSPD.

The wide nanowires of detector TaN-B allow for a certain energy-resolving capability (as also demonstrated for the Nb X-SNSPD) in contrast to the narrower nanowires of TaN-A (Fig. 14.2). This observation proves, that small normal-domain resistances are responsible for energy-dependent photon-detection pulse amplitudes. However, the wider nanowires of TaN-B also limit the DDE at low temperatures, which can be explained within a standard hot-spot model [3]. Increasing

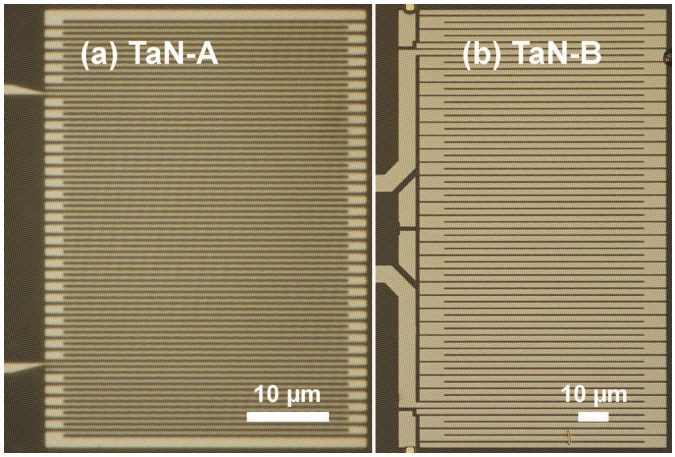

FIG. 14.1 – Optical images of the examined X-SNSPDs from 100 nm thick TaN [2]:
(a) TaN-A with $w \simeq 310$ nm and
(b) TaN-B with $w \simeq 1.85$ μm wide nanowires.

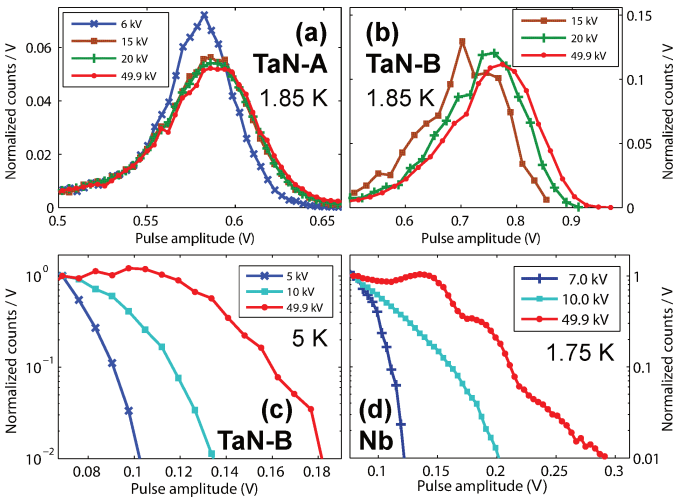

FIG. 14.2 – Pulse-amplitude histograms for different X-ray tube acceleration voltages [2]
(a) TaN-A (at $I_b = 54$ μA)
(b) TaN-B (at $I_b = 243$ μA)
(c) TaN-B (at $I_b = 121$ μA) at elevated temperature
(d) the Nb X-SNSPD (at I_b=0.61 mA)
The distributions in (a) and (b) are normalized to the total number of events, those in (c) and (d) to the counts at 69 and 79 mV, respectively.

the operation temperature increases the DDE but also reduces the pulse amplitude due to a decreasing critical current.

We have also achieved important progress on conventional optical SNSPD in the reporting period. There has been growing evidence in recent years that magnetic vortices are the dominating source of fluctuation-based dark-count events in optical SNSPD [4, 5]. Therefore it is obvious to expect a certain dependence of the dark-count rate on an applied magnetic field [6]. This dependence is expected to be symmetric with respect to the direction of the magnetic field perpendicular to the detector plane and the bias-current direction. However, our measurements revealed a surprising asymmetry with respect to the sign change of the magnetic field [7], which we successfully explained by a current-crowding effect in inequivalent corners of the meander shape [8].

In another series of experiments we have for the first time systematically studied the temperature-dependent performance of SNSPD [9]. Our data confirmed what has long been observed: SNSPD not only have a reduced dark-count rate when operated at temperatures below 4 K, but also an increased cut-off wavelength. We could qualitatively explain this surprising behavior by taking into account a temperature-dependent diffusion coefficient for quasi-particles that enters the standard detection model [10].

14.2 Thermodynamic signature of vortex-lattice melting

In type-II superconductors, an external magnetic field penetrates a superconductor in form of magnetic flux lines which arrange themselves in a regular lattice, each one carrying one magnetic flux quantum $\Phi_0 = 2.07 \times 10^{-15}$ Vs. This lattice has been shown to show a first-order melting transition in high-temperature cuprate superconductors $YBa_2Cu_3O_7$ [11] and $Bi_2Sr_2CaCu_2O_8$ [12]. A temperature-driven phase transition of the vortex lattice should, in principle, also occur in sufficiently clean low-temperature superconductors. For Nb, attempts have been made to measure the melting entropy directly, and the absence of a related signal in very pure samples has led to reflections about the complete absence of vortex-lattice melting in this compound [13].

Based on available literature to describe the vortex-state and using the Lindemann criterion, we have determined the melting lines and the related melting entropies, to be able to judge on the compatibility of experimental data with the theoretical predictions, using a few known material parameters.

The Lindemann criterion is based on the idea that melting occurs as soon as the thermal mean-square displacements $\langle u_{th}^2 \rangle^{1/2}$ of the of atoms (or in our case vortices) in a lattice reaches a certain fraction of the lattice constant $a = \sqrt{\Phi_0/B}$, i.e., $\langle u_{th}^2 \rangle^{1/2} \simeq c_L a$ with the Lindemann number $c_L < 1$. Corresponding quantitative calculations for the vortex-lattice melting lines lead to an implicit equation [14]

$$\frac{t_m}{\sqrt{1-t_m^2}} = \frac{2\pi c_L^2}{Gi^{1/2} b^{1/2} f(b)}, \tag{14.2}$$

with $t_m = T_m/T_{c0}$ the reduced melting temperature T_m for $B = B_m$ with respect to the critical temperature T_{c0} in zero magnetic field, $b = B/B_{c2}(T)$ the reduced magnetic induction B with respect to the temperature dependent upper-critical field $B_{c2}(T)$, and Gi the Ginzburg number of the superconductor. Within a collective pinning theory [14], the function $f(b)$ is

$$f(b) = \frac{2\beta_A \sqrt{1+(1+c(b))^2} - 1}{(1-b)c(b)(1+c(b))}, \tag{14.3}$$

valid for all values of b throughout the mixed state, with $c(b) = \sqrt{\beta_A(1-b)}/2$ and $\beta_A = 1.16$ the Abrikosov number (other theoretical approaches produce similar results for $f(b)$). In Fig. 14.3 we show the corresponding melting lines according to Eq. (14.2), evaluated for a number of different type-II superconductors.

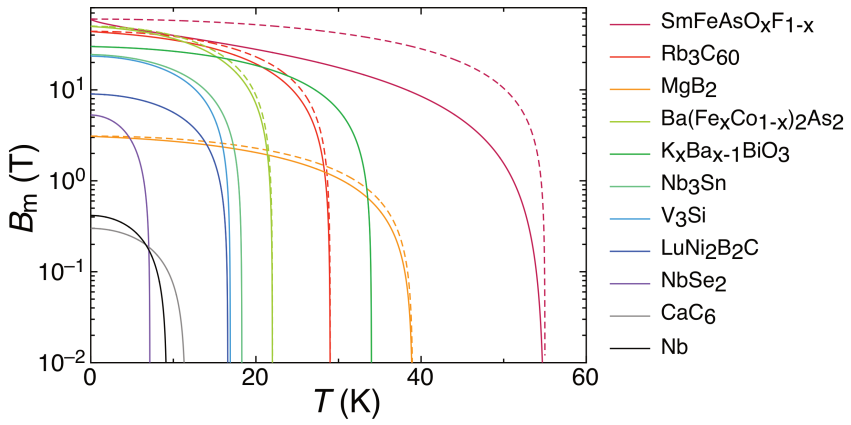

FIG. 14.3 – Expected melting lines $B_m(T)$ for various type-II superconductors, calculated from Eqs. (14.2) and (14.3) with $c_L = 0.20$. The $B_{c2}(T)$-lines (dotted lines) have been plotted only for SmFeAsO$_x$F$_{1-x}$, Rb$_3$C$_{60}$, MgB$_2$, and Ba(Fe$_x$Co$_{1-x}$)$_2$As$_2$ for which they appear distinct from $B_m(T)$ in this representation.

To obtain the melting entropies, we made use of Richard's rule for crystal lattices, in which the configurational melting entropy per particle is assumed to be a constant multiple (or fraction) of k_B. With the volume V_0 occupied by one particle we then have

$$\Delta s_0 V_0 = \eta k_B, \tag{14.4}$$

where Δs_0 is the configurational melting entropy per volume and η is an unknown constant on the order of 1. Using a result by Kierfeld and Vinokur [15], the volume V_0 is

$$V_0 = \frac{\varepsilon a^3}{\sqrt{1-b}}. \tag{14.5}$$

It turned out that the entropy obtained from applying Richard's rule alone considerably underestimates the measured entropy changes Δs upon vortex-lattice melting both in $YBa_2Cu_3O_7$ and in $Bi_2Sr_2CaCu_2O_8$ [16]. Taking the marked temperature dependence of thermodynamic quantities into account, Dodgson *et al.* arrive at an enhancement of Δs_0 of the form [16]

$$\Delta s = \frac{[1-\tilde{b}+(2\tilde{b}-t^2)t^2]}{(1-t^2-\tilde{b})(1-t^2)}\Delta s_0, \tag{14.6}$$

with $\tilde{b} = B/B_{c2}(0)$. We have calculated $\Delta s/\eta$ for the compounds analyzed in Fig. 14.3 using Eqs. (14.4) and (14.6) (see Fig. 14.4).

The resulting discontinuities in the magnetization can be derived from the Clausius-Clapeyron equation,

$$\Delta s = -\Delta M \frac{\mathrm{d}B_m}{\mathrm{d}T}, \tag{14.7}$$

with $\Delta M > 0$, i.e., M increases when crossing $B_m(T)$ from the solid to the "liquid" phase. The results of this calculation are displayed in Fig. 14.5.

These magnetization discontinuities ($4\pi\Delta M \simeq 8$ mG to 0.11 G, in cgs-units) are small, but they should still be within the sensitivity specifications of commercial SQUID magnetometers [17]. Moreover, the Δs of the calculated magnitude should, in principle, also be measurable in high-quality single crystals provided that thermodynamic equilibrium is achieved.

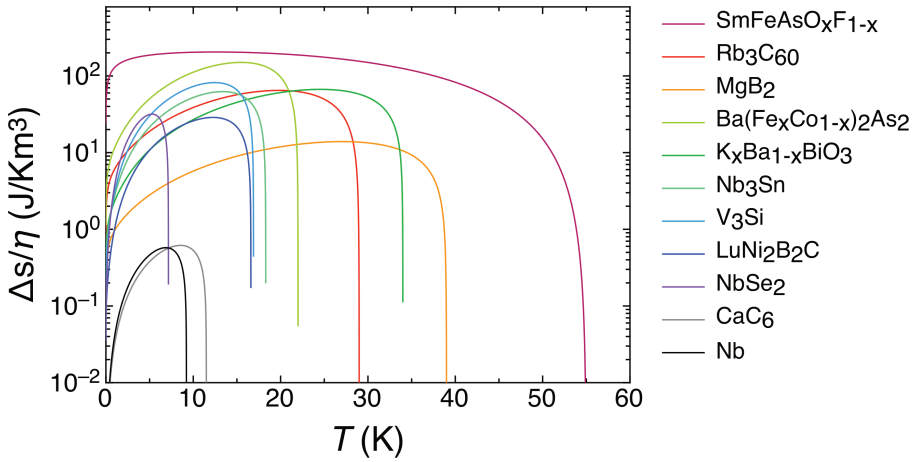

FIG. 14.4 – Vortex-lattice melting entropies $\Delta s/\eta$ for various type-II superconductors at the $B_m(T)$ shown in Fig. 14.3, as a function of T.

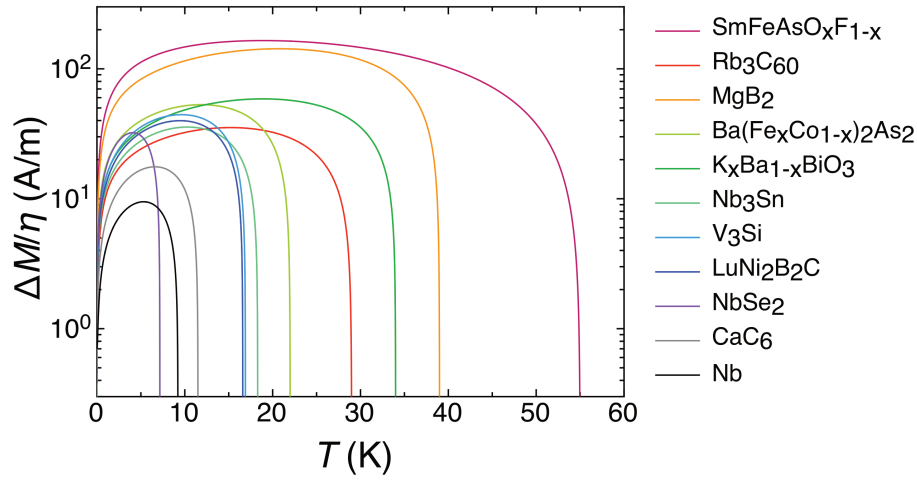

FIG. 14.5 – Discontinuities $\Delta M/\eta$ in magnetization at the $B_m(T)$ of the materials under discussion.

14.3 Material considerations for BEC in magnetic insulators

In the previous annual report, we have suggested to probe the existence of macroscopic phase coherence in so called triplon Bose-Einstein condensates (BEC) that are supposed to form in certain magnetic insulators, with a novel experimental scheme [18]. The proposal is based on using two coupled materials with slightly different chemical potentials for the respective triplon quasiparticles, representing an analogue to a Josephson device for superconductors. The a.c. Josephson effect should then manifest itself in a distinct change of the respective energy spectra. As the construction of such a device relies on the control of the material properties and the quality of the junctions, we decided to investigate two different prototype materials. The mother compounds of the solid solution $Ba_{3-x}Sr_xCr_2O_8$ (i.e. $x = 0$ and $x = 3$) have the same crystal structure but with different lattice parameters and different critical fields ($H_c = 12.5\,\mathrm{T}$ and $30\,\mathrm{T}$) [19, 20], potentially allowing for the fine-tuning of the magnetic interaction parameters through the stoichiometry. On the other hand, the preparation of Br-doped dichloro-tetrakis-thiourea-nickel (DTN) [22] with different Br contents could allow in a natural way to prepare coupled single crystals with different H_c's, thereby ensuring a high quality of the Josephson junction itself.

14.3.1 $Ba_{3-x}Sr_xCr_2O_8$ as a prototype material

We have synthesized several members of the solid solution $Ba_{3-x}Sr_xCr_2O_8$ and performed a detailed investigation of the structural and magnetic properties, in particular of the magnetic intradimer interaction constant J_d which is important for the strength of the critical field H_c [21]. Single crystals with $x = 0, 0.1$ and 3 (prepared by Hanna Dabkowska at McMaster University in Hamilton, Canada), as well as polycrystalline material with $0 \leq x \leq 3$ have been analyzed using a commercial SQUID magnetometer (*Quantum Design Inc.*). The resulting magnetization as a function of the temperature in the range of $2\,\mathrm{K} \leq T \leq 300\,\mathrm{K}$ was fitted using the Bleaney-Bowers formula for interacting dimers,

$$M_d(T) = \frac{n_\mathrm{d} g^2 \mu_\mathrm{B} B_\mathrm{ext}}{J_e + k_B T \left(3 + e^{\frac{J_\mathrm{d}}{k_B T}}\right)}, \qquad (14.8)$$

with an additional Brillouin term for the seemingly increasing paramagnetic background for $0.5 \leq x \leq 2$,

$$M_p(T) = n_P g \mu_\mathrm{B} \left(\coth\left(\frac{g\mu_\mathrm{B} B_\mathrm{ext}}{k_B T}\right) - \frac{1}{2}\coth\left(\frac{g\mu_\mathrm{B} B_\mathrm{ext}}{2k_B T}\right)\right).$$

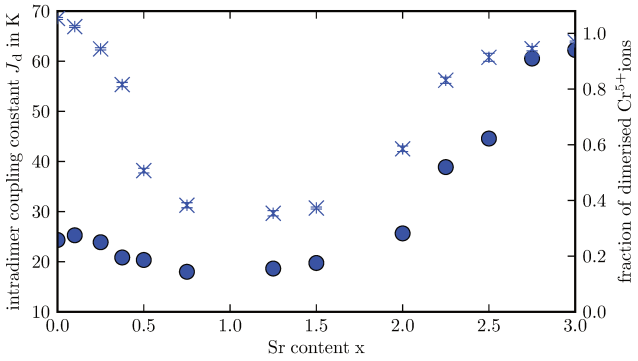

FIG. 14.6 – Estimated intradimer interaction constant J_d in $Ba_{3-x}Sr_xCr_2O_8$ (filled circles) and the fraction of dimerized Cr^{5+}-ions (crosses, prefactor n_d from Eq. 14.8), as a function of the strontium content x.

The thus obtained intradimer interaction constant J_d is shown in Fig. 14.6, together with the estimated fraction n_d of dimerized Cr^{5+} ions. The interaction constant has a broad minimum for intermediate values of x, possibly leading to a decrease of the critical field.

As the drop of the fraction of dimerized Cr^{5+} ions and, conversely, the increase of the paramagnetic background might indicate the presence of impurity phases, and to obtain further structural information about the solid solution, we performed powder-diffraction experiments using $Cu_{K\alpha}$ X-ray radiation on polycrystalline samples and crushed parts of single crystals mentioned above. The diffraction data were analyzed using a Rietveld method. We found the space group to remain the same as for the mother compounds ($R\bar{3}m$). As expected, the lattice constants vary smoothly as functions of x, whereas the atomic positions remain essentially unchanged. Surprisingly, the obtained spectra show no sign of impurity phases. We therefore conclude that the paramagnetic background is intrinsic to $Ba_{3-x}Sr_xCr_2O_8$ and may hint to the formation of unpaired Cr^{5+} ions by the presence of disorder, introduced by the partial substitution of Ba by Sr.

14.3.2 ESR-Experiments on DTN

To search for possible changes in the energy spectra of coupled magnetic insulators with different critical fields, ESR measurements were performed on samples of DTN ($NiCl_2{-}4SC(NH_2)_2$). A sample of pure DTN as well as a specimen of doped DTN with 13% of the Cl atoms replaced by Br, and a third, coupled sample, consisting of a core of pure DTN and a shell of DTN, doped with Br (samples prepared by Armando Paduan-Filho, University of São Paulo) were analyzed using ESR frequencies in the range of 290 GHz – 450 GHz in magnetic fields up to $\mu_0 H = 16\,\mathrm{T}$. At the writing of this report, only measure-

ments for the uncoupled specimens have been conducted in the temperature region of interest ($T \leq 1.2\,K$) (in collaboration with Vladislav Kataev and Alexey Alfonsov, IFW Dresden). We expect results for the coupled device by the end of this year.

14.3.3 Modeling disorder in the quantum magnet $Tl_{1-x}K_xCuCl_3$

Within a scientific visit of Prof. A. Rakhimov (Institute of Nuclear Physics, Tashkent, Uzbekistan) we have attempted to model the effect of crystalline disorder on the density of the triplon condensate in the quantum magnet $Tl_{1-x}K_xCuCl_3$, where the dopant K acts as a source of disorder. A standard formalism for atomic bosonic gases by Huang and Meng [23] turned out not to be satisfactory to fully explain the experimental data. The reason is that the parameters of the Hamiltonian of atomic gases are naturally fixed (*i.e.*, independent of weak disorder), while certain parameters in the Hamiltonian of spin gapped quantum magnets may change with doping, *e.g.*, due to a related variation of the magnetic-coupling energies with varying bond lengths as a function of x. Taking into account these modifications we finally found a good agreement between theory and experiment. Bond random effects in mixed magnetic spin systems manifest themselves in dual way: by modification of internal parameters and by localization on random scatterers. Each of these effects could be studied separately in an appropriate theory, but they should be taken into account simultaneously for an adequate description of, *e.g.*, measured magnetization data. The interplay between these effects leads to a nontrivial behavior of the sound-like speed c: when the external magnetic field H is fixed but x is experimentally varied, c increases for small x, reaches a maximum value and then decreases due to localization effects. While the speed of this mode was measured in dilute BEC of sodium atoms a long time ago, it has never been an intense focus of research in dimerized quantum magnets. It could be systematically studied, for example, by measuring the dispersion relation with inelastic neutron scattering techniques [24].

14.4 Novel Materials for Thermoelectrics and Topological Insulators

Recent studies have shown that $GeBi_4Te_7$ exhibits free-standing topological surface states [25]. Moreover, this material has been under consideration as a potentially good thermoelectric because of its large thermopower and the expected low lattice thermal conductivity due to the large, complex unit cell (see e.g. [26], [27]). For the systematic investigation of the physical properties

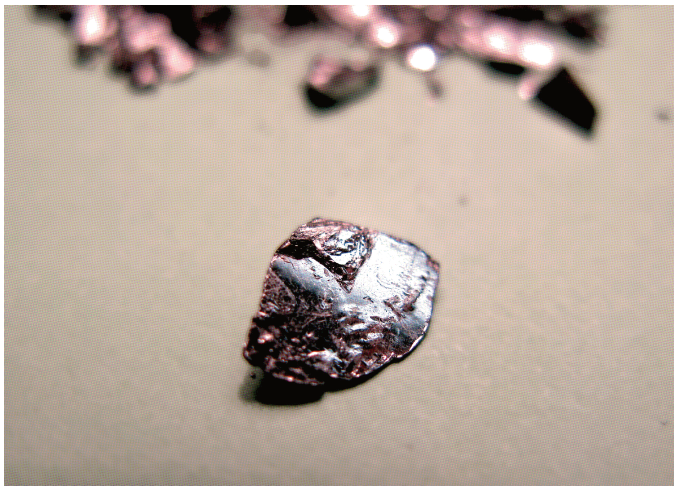

FIG. 14.7 – Photograph of as-grown single crystals of $GeBi_4Te_7$. Sizes are typically 10 mm.

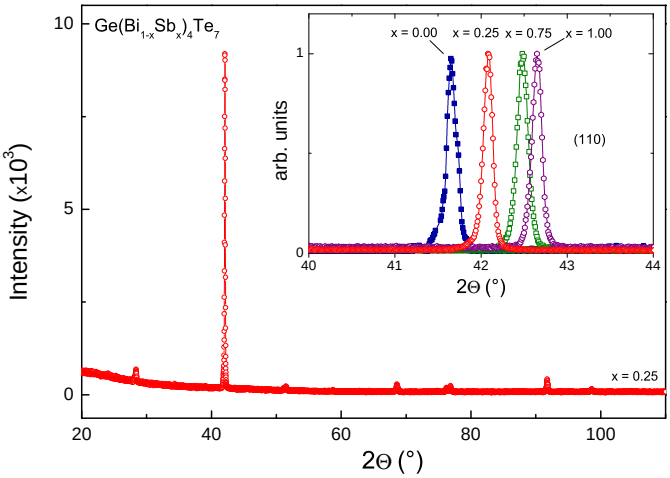

FIG. 14.8 – The X-ray diffraction pattern of $x = 0.25$ showing the reflections from the basal plane of the cleaved single crystal. In the inset we show the change of the (110) reflection for $x = 0$, 0.25, 0.75 and 1.

of this material, we have grown large single crystals of $GeBi_4Te_7$ and the $Ge(Bi_{1-x}Sb_x)_4Te_7$ solid solution by the modified Bridgman method. We have used the isovalent and isostructural substitution of Bi by Sb as a way to manipulate the Fermi-level of these compounds. The as-grown crystals of $GeBi_4Te_7$ are shown in Fig. 14.7. Powder X-ray diffraction patterns of all samples of the solid solution were indexed using the hexagonal space group $P\bar{3}m1$ and were found free of any impurity reflections. The XRD pattern for $x = 0.25$ and the change of the (110) reflection as a function of doping for $x = 0$, 0.25, 0.75 and 1 are shown in Fig. 14.8. Replacing Bi by Sb leads to a decrease of the unit-cell volume due to the smaller ionic radius of Sb. Within this series, the lattice parameters vary from approximately $a = 4.29$ Å, $c = 23.89$ Å for the pure Bi end member, to $a = 4.24$ Å, $c = 23.80$ Å for the pure Sb end member.

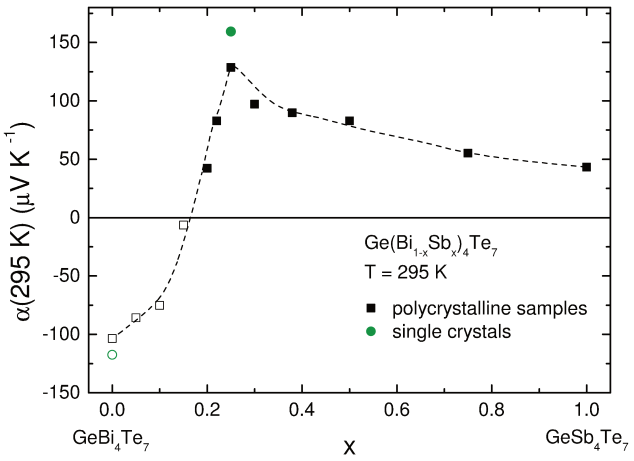

FIG. 14.9 – Composition dependence of the room temperature thermopowers of $Ge(Bi_{1-x}Sb_x)_4Te_7$ for x ranging from 0 to 1, for 12 differently doped polycrystalline samples, and two single crystals (x = 0 and 0.25). The dashed line is a guide to the eye for the room temperature thermopowers of the polycrystalline samples.

Our temperature dependent measurements of the thermopower $\alpha(T)$ in the range from 10 K to 300 K reveal a systematic crossover from n-type to p-type in $Ge(Bi_{1-x}Sb_x)_4Te_7$. The thermopower in this solid solution ranges from -117 μVK^{-1} to +160 μVK^{-1}. The crossover from n-type to p-type is continuous with increasing Sb content and occurs around $x \simeq 0.15$. The room temperature thermopowers α_{295K} of $Ge(Bi_{1-x}Sb_x)_4Te_7$ for the whole range from $x = 0$ to $x = 1$, measured for 12 differently doped polycrystalline samples and two single crystals, are shown in Fig. 14.9. The highest positive thermopowers are observed in the vicinity of the transition from n-type to p-type.

All samples show semimetallic behavior that is typical for heavily doped semiconductors, with electrical conductivities $\sigma(T)$ in the range from 150 to 2200 Scm^{-1}. We find that the crossover from n-type to p-type is not accompanied by a semiconducting or insulating resistivity regime. As a general trend, we observe that the electrical conductivity increases with increasing Sb content. The temperature dependent thermal conductivities $\kappa(T)$ range from 0.2 $WK^{-1}m^{-1}$ for $x = 0$ to 0.8 $WK^{-1}m^{-1}$ for $x = 1$, and increase as a function of Sb content. The highest resulting thermoelectric efficiencies among the tested n-type and p-type samples are $Z_nT = 0.11$ and $Z_pT = 0.20$, respectively. For an optimal n-p couple in this alloy system, the composite figure of merit is $Z_{np}T = 0.17$ at room temperature.

Our findings suggest a road to obtain better thermoelectric materials in this system [28]. Furthermore, the results indicate future pathways to optimization of the compound as both a thermoelectric and a topological insulator. In future work we will concentrate on the properties of the surface states in the vicinity of the n-p crossover, in collaboration with the group of Prof. Osterwalder at our institute.

[1] K. Inderbitzin, A. Engel, A. Schilling, K. Il'in and M. Siegel, Appl. Phys. Lett., **101** (2012), 162601.

[2] K. Inderbitzin, A. Engel and A. Schilling, IEEE Trans. Appl. Supercond., **23** (2013), 2200505.

[3] A. Gabutti, R. G. Wagner, K. E. Gray, R. T. Kampwirth and R. H. Ono, Nucl. Instrum. Methods A, **278** (1989), 425.

[4] H. Bartolf, A. Engel, A. Schilling, K. Il'in, M. Siegel, H.-W. Hübers and A. Semenov, Phys. Rev. B, **81** (2010), 024502.

[5] L. N. Bulaevskii, M. J. Graf, C. D. Batista and V. G. Kogan, Phys. Rev. B, **83** (2011), 144526.

[6] L. N. Bulaevskii, M. J. Graf and V. G. Kogan, Phys. Rev. B, **85** (2012), 014505.

[7] A. Engel, A. Schilling, K. Il'in and M. Siegel, Phys. Rev. B, **86** (2012), 140506(R).

[8] J. R. Clem, Y. Mawatari, G. R. Berdiyorov and F. M. Peeters, Phys. Rev. B, **85** (2012), 144511.

[9] A. Engel, K. Inderbitzin, A. Schilling, R. Lusche, A. Semenov, H.-W. Hübers, D. Henrich, M. Hofherr, K. Il'in and M. Siegel, IEEE Trans. Appl. Supercon., **23** (2013), 2300505.

[10] A. Semenov, A. Engel, H.-W. Hübers, K. Il'in and M. Siegel, Eur. Phys. J. B, **47** (2005), 495.

[11] A. Schilling, M. Willemin, C. Rossel, H. Keller, R. A. Fisher, N. E. Phillips, U. Welp, W. K. Kwok, R. J. Olsson and G. W. Crabtree, Phys. Rev. B **61** (2000), 3592.

[12] E. Zeldov, D. Majer, M. Konczykowski, V. B. Geshkenbein, V. M. Vinokur and H. Shtrikman, Nature **375** (1995), 373.

[13] C. J. Bowell, R. J. Lycett, M. Laver, C. D. Dewhurst, R. Cubitt and E. M. Forgan, Phys. Rev. B **82** (2010), 144508.

[14] G. P. Mikitik and E. H. Brandt, Phys. Rev. B **64** (2001), 184514.

[15] J. Kierfeld, Phys. Rev. B **69** (2004), 024501.

[16] M. J. W. Dodgson, V. B. Geshkenbein, H. Nordborg and G. Blatter, Phys. Rev. B **57** (1998), 14498.

[17] O. Bossen and A. Schilling, Physica C **483** (2012), 201.

[18] A. Schilling, H. Grundmann and R. Dell'Amore, Journal of Physics: Conference Series **400** (2012), 032081;
A. Schilling and H. Grundmann, Annals of Physics **327** (2012), 2301.

[19] A. A. Aczel, H. A. Dabkowska, P. R. Provencher and

G. M. Luke. Journal of Crystal Growth, **310** (2008), 870;
M. Kofu, H. Ueda, H. Nojiri, Y. Oshima, T. Zenmoto, K. C. Rule, S. Gerischer, B. Lake, C. D. Batista, Y. Ueda and S.-H. Lee, Phys. Rev. Lett., **102** (2009), 177204.

[20] E. Cuno and H. Müller-Buschbaum, Z. anorg. allg. Chemie, **572** (1989), 95; A. A. Aczel, Y. Kohama, C. Marcenat, F. Weickert, M. Jaime, O. E. Ayala-Valenzuela, R. D. McDonald, S. D. Selesnic, H. A. Dabkowska and G. M. Luke, Phys. Rev Lett., **103** (2009), 207203.

[21] H. Grundmann, A. Schilling, C. A. Marjerrison, H. A. Dabkowska and B. D. Gaulin, under review in Material Research Bulletin.

[22] V. Zapf, D. Zocco, B. R. Hansen, M. Jaime, N. Harrison, C. D. Batista, M. Kenzelmann, C. Niedermayer, A. Lacerda and A. Paduan-Filho, Phys. Rev. Lett., **96** (2006), 077204.

[23] K. Huang and H. F. Meng, Phys. Rev. Lett., **69** (1992), 644.

[24] A. Rakhimov, S. Mardonov, E. Ya. Sherman and A. Schilling, New J. Phys., **14** (2012), 113010.

[25] S.-Y. Xu, *et al.*, ArXiv e-prints 1101.3985, (2011).

[26] L. Shelimova, P. Konstantinov, M. Kretova, E. Avilov and V. Zemskov, Inorganic Materials, **40** (2004), 461.

[27] V. Kuznetsov, L. Kuznetsova, D. Rowe, J. Appl. Phys., **85** (1999), 3207.

[28] F. von Rohr, A. Schilling and R. J. Cava, J. Phy.: Cond. Matt., **25** (2013), 075804.